ERDC MP-21-7

Engineer Research and Development Center

US Army Corps of Engineers®
Engineer Research and Development Center

ERDC
ENGINEER RESEARCH & DEVELOPMENT CENTER

Machine-Learning of Long-Range Sound Propagation through Simulated Atmospheric Turbulence

Carl R. Hart, D. Keith Wilson, Chris L. Pettit, and Edward T. Nykaza

July 2021

Approved for public release; distribution is unlimited.

The U.S. Army Engineer Research and Development Center (ERDC) solves the nation's toughest engineering and environmental challenges. ERDC develops innovative solutions in civil and military engineering, geospatial sciences, water resources, and environmental sciences for the Army, the Department of Defense, civilian agencies, and our nation's public good. Find out more at www.erdc.usace.army.mil.

To search for other technical reports published by ERDC, visit the ERDC online library at https://erdclibrary.on.worldcat.org/discovery.

ERDC MP-21-7
July 2021

Machine-Learning of Long-Range Sound Propagation Through Simulated Atmospheric Turbulence

Carl R. Hart and D. Keith Wilson

Cold Regions Research and Engineering Laboratory
U.S. Army Engineer Research and Development Center
72 Lyme Road
Hanover, NH 07355

Chris L. Pettit

Aerospace Engineering Department
U.S. Naval Academy
Annapolis, MD 21402

Edward T. Nykaza

Construction Engineering Research Laboratory
U.S. Army Engineer Research and Development Center
2902 Newmark Drive
Champaign, IL 61822

Final report

Prepared for U.S. Army Corps of Engineers
Washington, DC 20314

Under Program Element Number 611102, Project AB2, Task 01

Preface

This study was conducted for the U.S. Army Corps of Engineers ERDC Geospatial Research Engineering basic research program under Program Element Number 611102, Project AB2, Task 01. The technical monitor was Mr. Robert E. Davis.

The work was performed by the Signature Physics Branch (Dr. Marino A. Niccolai, Chief) of the Research and Engineering Division (Dr. George W. Calfas, Acting Chief), U.S. Army Engineer Research and Development Center, Cold Regions Research and Engineering Laboratory (ERDC-CRREL) and by the Environmental Processes Branch (Mr. Jeff Burkhalter, Acting Chief) of the Installations Division (Ms. Giselle Rodriguez, Chief), U.S. Army Engineer Research and Development Center, Construction Engineering Research Laboratory (ERDC-CERL). At the time of publication, the Deputy Director of ERDC-CRREL was Mr. David B. Ringelberg, and the Director was Dr. Joseph L. Corriveau. The Acting Deputy Director of ERDC-CERL was Ms. Michelle Hanson and the Director was Dr. Andrew Nelson.

This article was originally published online in the *Journal of the Acoustical Society of America* on 21 June 2021. This paper is part of a special issue on Machine Learning in Acoustics. We extend much appreciation to the ERDC team responsible for the measurements used in this paper. In particular, the authors thank Michael J. White (ERDC-CERL) for code that computed peak pressure and positive phase duration of C4 detonations.

The Commander of ERDC was COL Teresa A. Schlosser and the Director was Dr. David W. Pittman.

Machine-learning of long-range sound propagation through simulated atmospheric turbulence

ABSTRACT:
Conventional numerical methods can capture the inherent variability of long-range outdoor sound propagation. However, computational memory and time requirements are high. In contrast, machine-learning models provide very fast predictions. This comes by learning from experimental observations or surrogate data. Yet, it is unknown what type of surrogate data is most suitable for machine-learning. This study used a Crank-Nicholson parabolic equation (CNPE) for generating the surrogate data. The CNPE input data were sampled by the Latin hypercube technique. Two separate datasets comprised 5000 samples of model input. The first dataset consisted of transmission loss (TL) fields for single realizations of turbulence. The second dataset consisted of average TL fields for 64 realizations of turbulence. Three machine-learning algorithms were applied to each dataset, namely, ensemble decision trees, neural networks, and cluster-weighted models. Observational data come from a long-range (out to 8 km) sound propagation experiment. In comparison to the experimental observations, regression predictions have 5–7 dB in median absolute error. Surrogate data quality depends on an accurate characterization of refractive and scattering conditions. Predictions obtained through a single realization of turbulence agree better with the experimental observations.
https://doi.org/10.1121/10.0005280

I. INTRODUCTION

Long-range outdoor sound propagation is characterized by a large variation in sound pressure levels (SPLs) over space and time (Valente *et al.*, 2012; Wilson *et al.*, 2015). The large variance is mainly attributed to meteorological effects (Embleton, 1996), which translate into sound speed variations in the atmosphere. Gradients of temperature and wind speed affect the refractive state of the atmospheric boundary layer (Bass, 2003) and atmospheric turbulence, resulting from wind velocity and temperature fluctuations, scatters the sound (Wilson *et al.*, 1999).

Whereas conventional numerical methods for outdoor sound propagation (Salomons, 2001) simulate a large variation in SPLs at long ranges, they may be costly in computational memory and time. Generating statistically consistent turbulence models (Wilson, 2000) for inclusion in such predictions is a time-consuming and memory intensive process. For example, in this study, several days are required to generate 5000 propagation simulations through single realizations of turbulence. Therefore, alternative prediction approaches are desirable.

Machine-learning models in acoustics (Bianco *et al.*, 2019) are a promising approach to efficiently predict outdoor sound propagation (Hart *et al.*, 2016). Earlier studies used a variety of statistical learning methods, including an artificial neural network (NN) model (Mungiole and Wilson, 2006), a cluster-weighted (CW) model (Pettit and Wilson, 2007), and a geostatistical model (Baume *et al.*, 2009). Although not a fundamental restriction, common to all of these studies is a maximum range of one kilometer and the omission of atmospheric turbulence.

The aim of this study is to quantify the accuracy of three machine-learning models for long-range (beyond 1 km) sound propagation while simultaneously considering atmospheric turbulence. A synthetic dataset is generated by a narrow-angle Crank-Nicholson parabolic equation (CNPE) model, which is described in Sec. II. The synthetic dataset serves as training and testing data for three machine-learning algorithms, which are described in Sec. III. The errors of these models with respect to an experimental long-range sound propagation dataset are discussed in Sec. IV. Finally, the viability of the machine-learning models, shown herein, for long-range outdoor sound propagation is summarized in Sec. V.

TABLE I. Parameters of synthetic dataset.

Variable	Symbol	Units
Frequency	f	Hz
Source height	z_s	m
Wind direction	α	deg
Friction velocity	u_*	m/s
Roughness height	z_0	m
Boundary-layer depth	z_i	m
Static flow resistivity	σ	N s/m^4
Porosity fraction	Ω	m^3/m^3
Sensible heat flux	H_s	W/m^2

II. SYNTHETIC DATASET

A. Parameter sampling

The challenge of developing a synthetic dataset for outdoor sound propagation is to sufficiently sample the relevant parameter space, which includes a multiplicity of propagation geometries, boundary conditions, and meteorological conditions. A practical approach for exploring the available parameter space is to use a sampling strategy. In this study, Latin hypercube sampling (LHS) is used because it facilitates even coverage of the parameter space (McKay *et al.*, 1979). Comprising this space are physically independent parameters that specify the conditions for an ensemble of propagation simulations.

Table I lists the parameters and their units for the present outdoor sound propagation simulations. Frequency and source height specify the continuous wave emitted by a point source and its position, respectively. Wind direction, friction velocity, roughness height, and sensible heat flux specify the mean profiles of the wind speed, temperature, and humidity (Bowen ratio is 0.5, a value characteristic of grasslands and forests) along the propagation path by Monin-Obukhov similarity theory (MOST; Ostashev and Wilson, 2016, pp. 35–38). Friction velocity, sensible heat flux, and boundary-layer height determine the length scales and variances for the von Kármán spectra of the temperature fluctuations, shear-induced velocity fluctuations, and buoyancy-induced velocity fluctuations (Ostashev and Wilson, 2016, pp. 202–204). These variances and length scales are input to a generalized random-phase model for synthetic turbulence with statistics that are constant in the range direction but vary in the vertical direction (Ostashev and Wilson, 2016, pp. 321–325). The variances and length scales for temperature and shear-driven velocity fluctuations vary throughout the height of the computational domain, but it may be more appropriate to set a constant value above the nominal height of the atmospheric surface layer. This is a topic for future research. Last, static flow resistivity and porosity establish properties for the acoustic impedance of the boundary. A relaxation impedance model (Wilson, 1993) provides the acoustic impedance and wavenumber of the flat ground by assuming a pore shape factor of one, and tortousity equal to the quartic root of porosity (Attenborough *et al.*, 2011).

Considering each parameter as an independent random variable, samples are drawn from the assumed distributions by LHS. Statistical parameters of each distribution and the type of distribution are given in Table II. Limits, means, and variances are assumed for each physical parameter with the exception of the frequency, source height, and wind direction. Instead, the limits and sampling distribution are assumed, which dictate the mean and variance. In particular, let frequency be considered a continuous random variable, $x_f \in [a_f, b_f]$, and $y_f = \log_{10} x_f$. The log-uniform distribution is

$$p(y_f | a_f, b_f) = \frac{1}{\log_{10}(b_f/a_f)}, \tag{1}$$

for $y_f \in [\log_{10}(a_f), \log_{10}(b_f)]$, zero otherwise. Random samples are drawn from this log-uniform distribution and transformed back to x_f. The mean and variance of the source frequency are, respectively,

$$\mu_f = \frac{b_f - a_f}{(\ln 10)\log_{10}(b_f/a_f)}, \tag{2}$$

$$\sigma_f^2 = \frac{b_f^2 - a_f^2}{(2\ln 10)\log_{10}(b_f/a_f)} - \left[\frac{b_f - a_f}{(\ln 10)\log_{10}(b_f/a_f)}\right]^2. \tag{3}$$

Uniform distributions are sampled for the source height and wind direction. For example, the mean and variance of the wind direction $\alpha \in [a_\alpha, b_\alpha]$ are $\mu_\alpha = (b_\alpha + a_\alpha)/2$ and

TABLE II. Assumed distributions randomly sampled for parameters of Table I. The means and variances of the frequency, source height, and wind direction are set by minimum and maximum values.

Variable	Minimum	Maximum	Mean	Variance	Distribution
Frequency	20	200	78.2	2488	Log-uniform
Source height	0	20	10	33.3	Uniform
Wind direction	0	180	90	2700	Uniform
Friction velocity	0.05	1	0.3	0.01	Beta
Roughness height	0.001	0.1	0.015	1×10^{-4}	Beta
Boundary-layer depth	200	2000	800	9×10^4	Beta
Static flow resistivity	3×10^4	3×10^7	1×10^6	5.625×10^{11}	Beta
Porosity fraction	0.2	0.7	0.45	0.01	Beta
Sensible heat flux	−20	1200	300	4×10^4	Beta

$\sigma_\alpha^2 = (b_\alpha - a_\alpha)^2/12$ (Bishop, 2006, p. 692). The limits, mean μ, and variance σ^2 are assumed for each of the remaining physical parameters. Each is considered as a continuous random variable $x \in [a, b]$, which undergoes a change of variable $y = (x - a)/(b - a)$. The samples are drawn from a beta distribution (Bishop, 2006, p. 686)

$$p(y|a', b') = \frac{\Gamma(a' + b')}{\Gamma(a')\Gamma(b')} y^{a'-1}(1 - y)^{b'-1}, \tag{4}$$

where $a' = \nu'\mu'$, $b' = (1 - \mu')\nu'$, $\mu' = (\mu - a)/(b - a)$, $\nu' = \mu'(1 - \mu')/\sigma'^2 - 1$, and $\sigma'^2 = \sigma^2/(b - a)$.

B. Simulation

The transmission loss (TL) for a harmonic point source over flat homogeneous terrain is predicted here using a CNPE model (West *et al.*, 1992). Simulations described here follow the modeling procedures of Hart *et al.* (2016) and Ostashev and Wilson (2016, pp. 404–410). The atmospheric domain spans 10 km in range and 2 km in height, which is resolved by the CNPE to one-tenth of a wavelength in both the height and range. Above the atmospheric domain is a 40 wavelength absorbing boundary. In addition to the computational grid, a coarser grid discretizes the mean and turbulent atmospheric fields. The resolution of this grid is one-half wavelength in height and ten wavelengths in range, which is sufficient for accurate computations (Wilson *et al.*, 2009). The TL is interpolated from the computational grid to this coarser grid. The TL is defined as

$$\mathrm{TL}(f, \mathbf{r}) = 20 \log_{10}\left[\frac{p_0(f)}{p(f, \mathbf{r})}\right], \tag{5}$$

where p_0 is the root mean square (RMS) acoustic pressure observed at a distance of 1 m in the free space, p is the RMS acoustic pressure at the receiver, f is the frequency of the source, and $\mathbf{r} = (r, z)$ are the coordinates of the receiver in terms of the range and height. The TL is converted to excess attenuation (EA),

$$\mathrm{EA}(f, \mathbf{r}) = \mathrm{TL}(f, \mathbf{r}) - 20 \log_{10}\left[\frac{|\mathbf{r} - \mathbf{r}_s|}{|\mathbf{r}_0|}\right], \tag{6}$$

where $\mathbf{r}_s = (0, z_s)$ are the coordinates of the source, $|\mathbf{r}_0| = 1$ m, and $|\mathbf{r} - \mathbf{r}_s|$ is the distance from the source to receiver in meters,

$$|\mathbf{r} - \mathbf{r}_s| = \sqrt{(z - z_s)^2 + r^2}. \tag{7}$$

Input to the CNPE model is based on the set of sampled parameters that are shown in Table I. Propagation through a single realization of synthetic turbulence under a very strong upward refracting condition and strong downward refracting condition are shown for 2 of the 5000 realizations in Fig. 1.

C. Derived parameters

In addition to the sampled parameters (see Table I), several predictors for machine-learning are derived from propagation physics and atmospheric variables. The derived parameters are summarized in Table III. Variables implicit in Table III include ρ_0 for the density of air, c_p for the specific heat of air at a constant pressure, $Q_s = H_s/\rho_0 c_p$ for the kinematic heat flux, g for gravitational acceleration, $\mathrm{Pr}_t = 0.95$ for the turbulent Prandtl number, T_0 for the surface temperature, c_0 for the sound speed in an ideal gas, $c_* =$

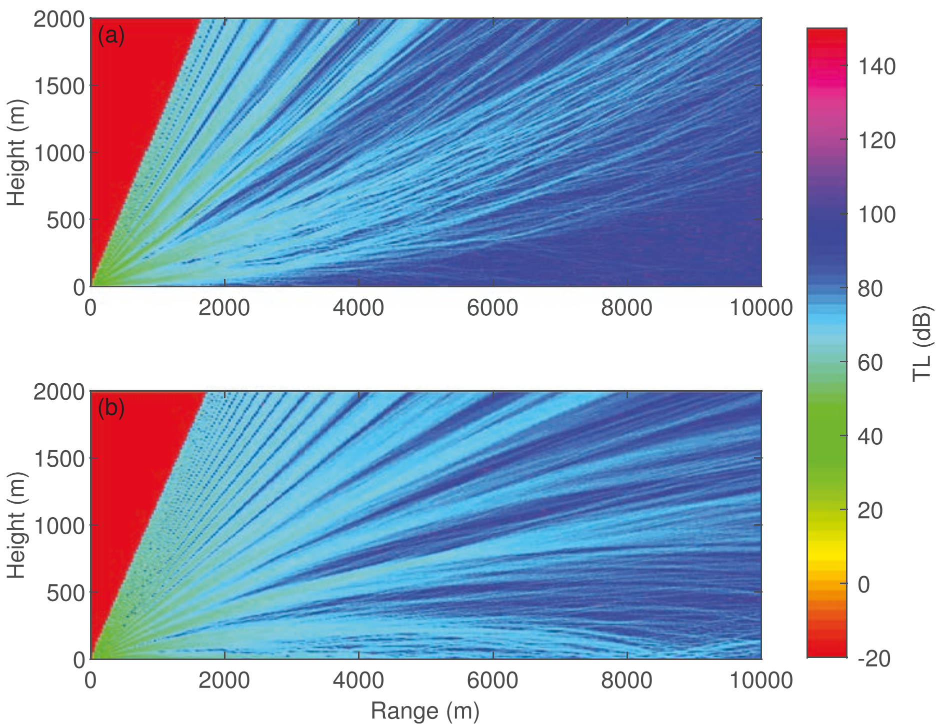

FIG. 1. (Color online) Transmission loss (TL) fields predicted by a CNPE model for (a) very strong upward refraction, where the source frequency is 104 Hz and effective sound speed scale is −3.09 m/s; (b) strong downward refraction, where the source frequency is 120 Hz and effective sound speed scale is 0.367 m/s. Other model parameters were sampled from distributions given by Table II.

TABLE III. Parameters derived from atmospheric variables and propagation physics.

Variable	Equation/symbol	Units
Normalized characteristic impedance magnitude	$\|Z_n\|$	rayl/rayl
Projected friction velocity	$(u_*)_\alpha = u_* \cos(\alpha)$	m/s
Surface-layer temperature scale	$T_* = -Q_s/u_*$	K
Mixed-layer velocity scale	$w_* = (gQ_s z_i/T_0)^{1/3}$	m/s
Effective sound speed scale	$c^*_{\mathrm{eff}} = c_* + (u_*)_\alpha/\mathrm{Pr_t}$	m/s
Obukhov length	$L_o = T_0 u_*^2/\kappa g T_*$	m
Inverse Obukhov length	L_o^{-1}	1/m
Shear-driven velocity fluctuation variance	$\sigma_s^2 = 3.0u_*^2$	$\mathrm{m^2/s^2}$
Buoyancy-driven velocity fluctuation variance	$\sigma_b^2 = 0.35w_*^2$	$\mathrm{m^2/s^2}$
Temperature fluctuation variance	σ_T^2; see Eq. (8)	$\mathrm{K^2}$
Shear-driven velocity fluctuation dissipation rate	$\epsilon_s = u_*^3/z\kappa$	$\mathrm{m^2/s^3}$
Shear-driven velocity fluctuation length scale	$l_s = 1.8z$	m
Temperature fluctuation length scale	l_T; see Eq. (9)	m

$(c_0/2T_0)T_*$ for the sound speed scale, and $\kappa = 0.4$ for the von Kármán constant. The normalized characteristic impedance magnitude is determined by the relaxation impedance model (Wilson, 1993). The projected friction velocity enters the definition for effective sound speed scale, which quantifies the strength of the effective sound speed gradient (Ostashev and Wilson, 2016, p. 95). The surface-layer temperature scale and Obukhov length are fundamental parameters for surface-layer similarity (MOST; Wyngaard, 2010, pp. 217–221). Correspondingly, the mixed-layer velocity scale is a fundamental parameter in mixed-layer similarity (Wyngaard, 2010, pp. 241–242). The inverse Obukhov length is an indicator of the mean meteorological profile shape (Ostashev and Wilson, 2016, p. 95). The velocity and temperature variances, dissipation rate, and length scales are all related to the von Kármán spectra of turbulence (Wilson, 2000). In particular, the bouyancy-driven velocity fluctuation variance is $\sigma_b^2 = 0.35w_*^2$. The shear-driven velocity fluctuation variance, dissipation rate, and length scale are $\sigma_s^2 = 3.0u_*^2$, $\epsilon_s = u_*^3/z\kappa$, and $l_s = 1.8z$, respectively. The variance of the temperature fluctuations is

$$\sigma_T^2 = \begin{cases} 4.0T_*^2[1+10(-z/L_o)]^{-2/3} & \text{if } Q_s > 0, \\ 4.0T_*^2 & \text{if } Q_s < 0, \end{cases} \tag{8}$$

and the temperature fluctuation length scale is

$$l_T = \begin{cases} 2.0z\dfrac{1+7(-z/L_o)}{1+10(-z/L_o)} & \text{if } Q_s > 0, \\ 2.0z & \text{if } Q_s < 0. \end{cases} \tag{9}$$

Because the buoyancy-driven velocity fluctuation length scale is directly proportional to the boundary-layer depth and both the buoyancy-driven velocity fluctuation dissipation rate and kinematic heat flux are directly proportional to the sensible heat flux, these variables are omitted from the model training. All of the derived parameters serve as additional training variables for each machine-learning model.

D. Dataset generation and filtering

It is unknown whether the surrogate data generated from propagation through single realizations of turbulence or an ensemble average of propagation through multiple realizations of atmospheric turbulence is most suitable for the machine-learning models. To explore this question, two datasets are generated, 1 for a single realization and another for ensemble averages from 64 realizations. The synthetic dataset is based on the EA sampled 1.5 m above the ground every 50 m in range between the source and 10 km for each simulation. For 5000 samples of parameters and 200 spatial points, each synthetic dataset, initially, is comprised of 1×10^6 values of the EA (TL).

Close to the source and for frequencies below 40 Hz, the EA values are incorrectly computed. This is potentially the result of spurious reflections from the top of the domain and narrow-angle approximation (Ostashev *et al.*, 2020). Therefore, only simulated observations from the 100 m range and further, along with frequencies of 40 Hz and greater, serve as the basis for the training and testing of each statistical learning model. A total of 695 505 and 697 296 values of the EA are retained for the single realization of turbulence and 64 realizations of turbulence datasets, respectively. Differences in the number of values retained result from random sampling of the model parameters.

III. MACHINE-LEARNING MODELS

Nonlinear regression of EA is developed by training three machine-learning models on each synthetic dataset. The three machine-learning models considered here are random forest (RF) regression, NN regression, and CW modeling. An earlier study showed that RF and NN models have high prediction skills for outdoor sound propagation (Hart *et al.*, 2016). Each of the three models contains two or more adjustable parameters, which are tuned by cross-validation, particularly by the validation set approach (James *et al.*, 2013). The dataset is split into a training dataset (75% of the observations chosen at random) and a test dataset (25% of the observations).

A. RF

RF regression is a type of ensemble decision tree model, which randomizes the sampled variables at each decision branch (Breiman, 2001). Decision trees are trained on bootstrapped datasets and the predictions are aggregated, which is otherwise known as *bagging*. One strategy for RF regression is to generate extensively grown decision trees, which have a high variance and low bias with respect to the out-of-bag error. An extensively grown decision tree partitions the parameter space finely, which results in many decision tree levels. Aggregating predictions of each decision tree then reduces the variance of the ensemble model (James *et al.*, 2013). The tuning parameters common to RF models are the number of variables to select, number of variables to sample at each decision branch, minimum terminal node size, and number of decision trees in the ensemble. In this order, the tuning parameters are adjusted. The initial settings for the variable selection step include: 200 decision trees, the number of variables to sample is the least integer for the square root in the number of variables, and a minimal terminal node size of 12.

Figure 2 shows the out-of-bag root mean square error (RMSE) as variables are eliminated by backward variable selection. Similar to backward stepwise regression, backward variable selection initially trains a RF model with all of the available training parameters and sequentially trains another model with one less variable until one variable remains. The variable eliminated at each stage is the one with the lowest variable importance, which is the increase in the mean square error when averaged over all trees in the ensemble and divided by the standard deviation taken over the trees, for each variable. The results of backward variable selection indicate that reducing the number of training parameters decreases the overall RMSE as variables are eliminated and then increases for four or fewer variables. In the case of RF models trained on the dataset corresponding to a single realization of turbulence, the minimum RMSE is for five variables. For training on the dataset with 64 realizations of turbulence, 8 variables result in the lowest RMSE, which is only 2/10 of a dB lower than the case for 23 variables (not shown). By backward variable selection, sets of five or fewer variables do not retain the source height. Because this parameter is an important physical characteristic, six variables corresponding to Fig. 2 are selected for the model training.

The variable importance for each of the six variables (predictors) from the backward selection is shown in Fig. 3. The variable importance is greatest for range. The variable importance for surface-layer temperature scale, projected

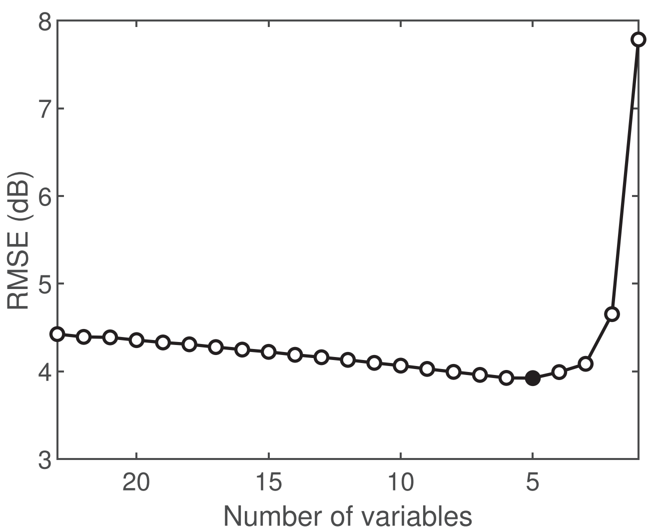

FIG. 2. The out-of-bag root mean square error (RMSE) of a random forest (RF) model trained with a decreasing number of input variables, according to the backward variable selection. The model was trained on a dataset corresponding to one realization of simulated turbulence. The solid marker corresponds to a model with the minimum RMSE.

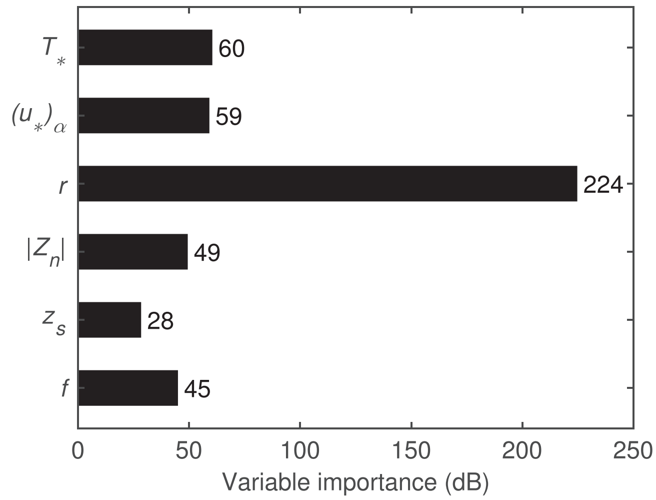

FIG. 3. The variable importance of a RF model trained with six input parameters. The model was trained on a dataset corresponding to one realization of simulated turbulence.

friction velocity, normalized characteristic impedance magnitude, and frequency are comparable, and approximately double in magnitude compared to source height.

Tuning the number of decision trees in the ensemble shows a convergence (less than 0.1% change) in the out-of-bag RMSE for 800 decision trees. For six variables, the minimum RMSE corresponds to five variables to sample at each decision branch. A minimum terminal node size of three data points results in the lowest RMSE. In consideration of the cross-validation results, a tuned RF model consists of 6 variables, 800 decision trees, 5 variables to sample at each decision branch, and 3 data points for the minimum terminal node size.

B. NN

NN models are suitable for nonlinear regression and may approximate the vast majority of functions when trained with a single hidden layer (Hornik *et al.*, 1989). Considered to be universal approximators, a network with one hidden layer and linear outputs is able to approximate any continuous function to arbitrary accuracy given enough hidden layer nodes (Bishop, 2006, pp. 230–231).

Cross-validation of NNs focused on one tuning parameter: the number of nodes in a single hidden layer of a network. Models were trained with the scaled conjugate gradient algorithm. A maximum of 5000 training iterations was allowed (in nearly every case, the training converged below this limit). The same six input variables as in the RF model were used. The number of hidden layer nodes leading to a minimum or near-minimum test RMSE is 55 nodes. A tuned NN contains 6 input nodes, 55 nodes in 1 hidden layer, and a single output node.

C. CW model

CW models infer the functional dependence between the observed input and output variables by joint density estimation using a flexible form of mixture modeling (Gershenfeld, 1999). This is accomplished by a process of updating forward and posterior probabilities according to the expectation maximization algorithm. The resulting regression model is similar to a moving least squares model.

The modeling choices for CW models include the form of the local model and number of clusters. Studies to date have used local models that were constant, linear, or quadratic. This study examined the use of the linear and quadratic models. Because CW models using the quadratic local model have a lower test RMSE than models trained with a linear local model, the quadratic local model without cross terms was selected here. The number of training parameters was set to the same six as used in the RF models. One complication of increasing the number of clusters indefinitely is the ill-conditioned nature of the least squares problem within the CW model estimation problem. For a quadratic local model, 6 training parameters and 13 clusters resulted in the lowest test RMSE without the least squares solution becoming ill-conditioned.

D. Test errors of machine-learning models

Figure 4 shows the distribution of absolute test errors for each machine-learned model trained on the dataset with a single realization of turbulence and another dataset with 64 realizations of turbulence. The median absolute error for models trained on the dataset with a single realization of turbulence is 3.8, 3.7, and 2.0 dB for the CW, NN, and RF models, respectively. The median absolute error for models trained on the dataset with 64 realizations of turbulence is 2.2, 2.0, and 1.2 dB for the CW, NN, and RF models, respectively. The median errors for the CW and NN models are similar. The RF models have the lowest median absolute errors and smallest range of outliers. The test RMSEs for the

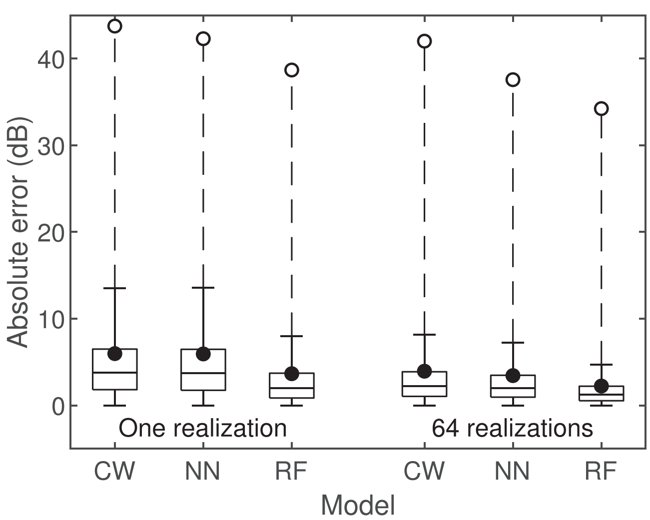

FIG. 4. The absolute test error aggregated over all cases for CW models, NN models, and RF models. The lower, middle, and upper lines of each box are the first, second, and third quantiles, respectively. The length of the upper whisker is 1.5 times the interquartile range. The dashed lines indicate the range of outliers. The maximum outliers are indicated by open circles. The RMSE for each model in the overall grouping is shown as solid circles.

RF models are 3.6 dB and 2.2 dB when trained on datasets with a single realization of turbulence and 64 realizations of turbulence, respectively.

IV. EXPERIMENTAL ERRORS OF MACHINE-LEARNING MODELS

A. Long-range sound propagation experiment

Next, consider the application of machine-learning techniques to a long-range sound propagation experiment conducted at the White Sands Missile Range in 2007 (Valente *et al.*, 2012). Over the course of ten days, testing uniformly sampled all 24 h of the day (dawn, day, dusk, and night). The experiment was conducted in the northwestern region of the range, which is characterized as a high desert plain with sandy soil and desert brush. Because the ground impedance was not measured during the course of the experiment, reasonable values must be estimated. Table III of Attenborough *et al.* (2011) enumerates several different ground types with grassland being the most pertinent. The porosity of grasslands ranges from 0.3 to 0.7 m^3/m^3, whereas the static flow resistivity ranges from 100 to 240 kPa s/m^2. Given a specific pair of porosity and static flow resistivity, the ground impedance is derived from the relaxation impedance model as described in Sec. II A. The geometry of the long-range sound propagation experiment was fixed throughout the test. The blast source was detonated at a height of 3 m. A distributed array of microphones, all at a height of 1.5 m, surrounded ground zero in a "Y"-like configuration. Microphones were spaced along the lines of the "Y" from 125 m to 16 km. Blast pencil gauges, at a height of 3 m were placed 4 m away from ground zero. This study will focus on measurements obtained on the east-north-east line of the "Y."

Because machine-learning models are trained on linear propagation data, it is important to evaluate the experimental range in which linear propagation prevails. During this experiment, a total of 218 detonations were initiated with composition C4. The blast wave propagates nonlinearly in the near field. Assuming that the source waveform follows a Friedlander pulse, it is possible to evaluate the peak SPL and positive phase duration under free-field conditions or consider the height of burst effect (Ford *et al.*, 1993). Particular attention is given to the range of 125 m as this was the range of the nearest microphone to ground zero. Figure 5 shows that for a 1.25 lb charge of C4 detonated 3 m above ground, the positive phase duration does not change at or beyond 125 m under free-field conditions. When considering the height of burst effect, the positive phase duration changes only slightly beyond 125 m. Figure 6 shows the measured peak SPLs at the 125 m site for 161 detonations passing quality assurance tests (Valente *et al.*, 2012). The majority of records indicate that peak SPLs were below the expected level due to the height of burst effect. Taken together, these observations indicate that linear propagation prevails from about 125 m and further in range.

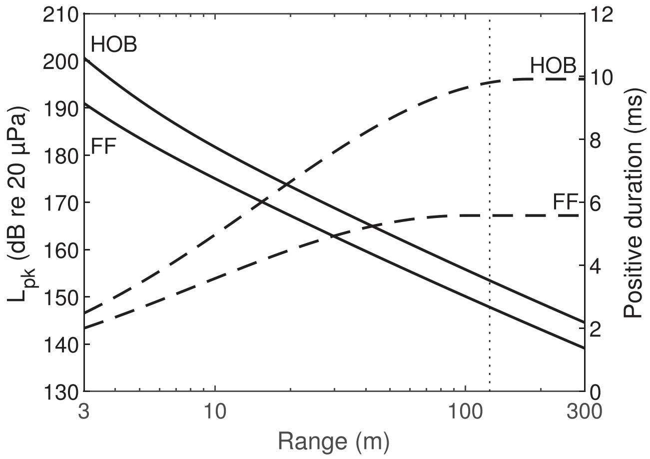

FIG. 5. The peak SPL (solid lines) and positive phase duration (dashed lines) as a function of the range for a 1.25 lb charge of C4. Differences in the peak SPL and positive phase duration are due to considering free-field propagation (FF) and the height of burst (HOB) effect. The vertical dotted line indicates a range of 125 m.

As experimental observations are in terms of unweighted sound exposure level (SEL), and machine-learning model predictions are in terms of EA, an indirect comparison is required. SEL is converted to SPL according to the integration time period associated with the SEL metric,

$$L_p(f,\mathbf{r}) = L_E(f,\mathbf{r}) - 10\log_{10}\left(\frac{T}{T_r}\right), \tag{10}$$

where L_E is unweighted SEL, T is the integration time period (3 s; Valente *et al.*, 2012), T_r is the reference integration time period (1 s), and L_p is unweighted SPL. The difference between the SPLs at two separate receivers is equivalent to the negative difference between the TL values,

$$\begin{aligned}\Delta\mathrm{TL} &= \mathrm{TL}(f,\mathbf{r}_2) - \mathrm{TL}(f,\mathbf{r}_1)\\ &= L_p(f,\mathbf{r}_1) - L_p(f,\mathbf{r}_2).\end{aligned} \tag{11}$$

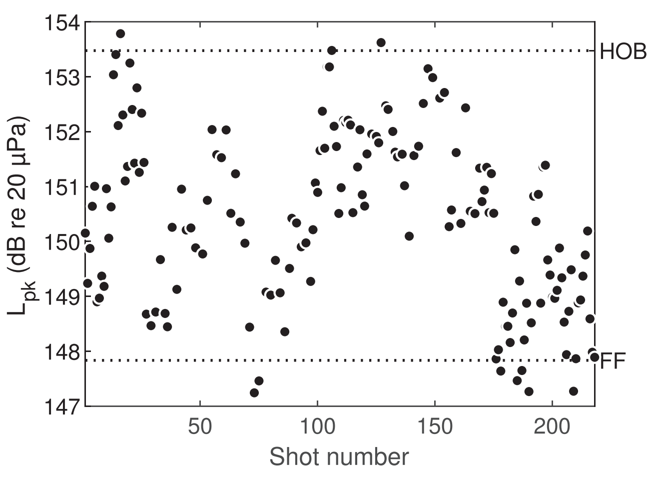

FIG. 6. The peak SPLs measured at a range of 125 m east-north-east of the blast site. The horizontal dotted lines are estimates for the peak SPL considering free-field propagation (FF) and the height of burst (HOB) effect.

Equivalently, the difference in the TL is the difference in the EA with a range correction factor,

$$\Delta\mathrm{TL} = \mathrm{EA}(f,\mathbf{r}_2) - \mathrm{EA}(f,\mathbf{r}_1) + 20\log_{10}\left(\frac{|\mathbf{r}_2-\mathbf{r}_s|}{|\mathbf{r}_1-\mathbf{r}_s|}\right). \tag{12}$$

The machine-learned models predict the EA, which is converted to differences in the TL between receivers at 1, 2, 4, and 8 km, and the 125 m range by Eq. (12). In each case, the height of the receiver is 1.5 m. The experimental observations are converted from the SEL to SPL and, then, the difference in the SPL at a range of $r_1 = 125$ m and the SPL of the $r_2 = 1$, 2, 4, and 8 km ranges is equated to the difference in the TL by Eq. (11).

A meteorological mast between the 1 and 2 km receiver ranges collected data that were used to determine the 30-min averages of the wind direction, friction velocity, and surface-layer temperature scale. The estimates for the friction velocity and temperature scale were iteratively estimated according to the procedure in Hart *et al.* (2018).

B. Comparisons between surrogate data and machine-learning models to experimental observations

Figure 7 shows the probability density function (PDF) estimates of the differences in the TL for both of the CNPE predictions, for one turbulence realization, and the experimental data. The PDF estimates are generated by normal kernel density estimation with a bandwidth optimal for estimating the normal densities (Bowman and Azzalini, 1997). The differences in the TL between 1 km and 125 m (150 m for the CNPE predictions due to the range interpolation intervals) are fairly similar with the mode of surrogate data being slightly less than experimentally observed and both characteristically skewed positively. At 2 km, the mode and variance of both are almost identical, taking on a nearly normal distribution. At 4 and 8 km, the variance and modes are underpredicted by the CNPE simulations and have little skew in comparison to the experimental data. Differences in the skew are a result of the relative amount of acoustic scattering in the real-world data. The positive skew can be attributed to a combination of direct and reflected sound propagation along with weak acoustic scattering (Bass *et al.*, 1991). When the distribution is skewed negatively, there is strong acoustic scattering (Dyer, 1970). The bias in ΔTL may be due to additional attenuation from nonlinear effects beyond 125 m. The underprediction of the variance in ΔTL at ranges of 4 and 8 km may be attributed to variations in real-world refractive conditions and excessive attenuation of simulated turbulence at increasing altitudes. By assuming Monin-Obukhov temperature and wind speed profiles throughout the simulation domain, the refractive state is not accurately characterized for stable nighttime conditions. This well-known shortcoming with MOST leads to gradients and downward refraction that are much too strong, and for ranges beyond 1 to 2 km, sound propagates above the

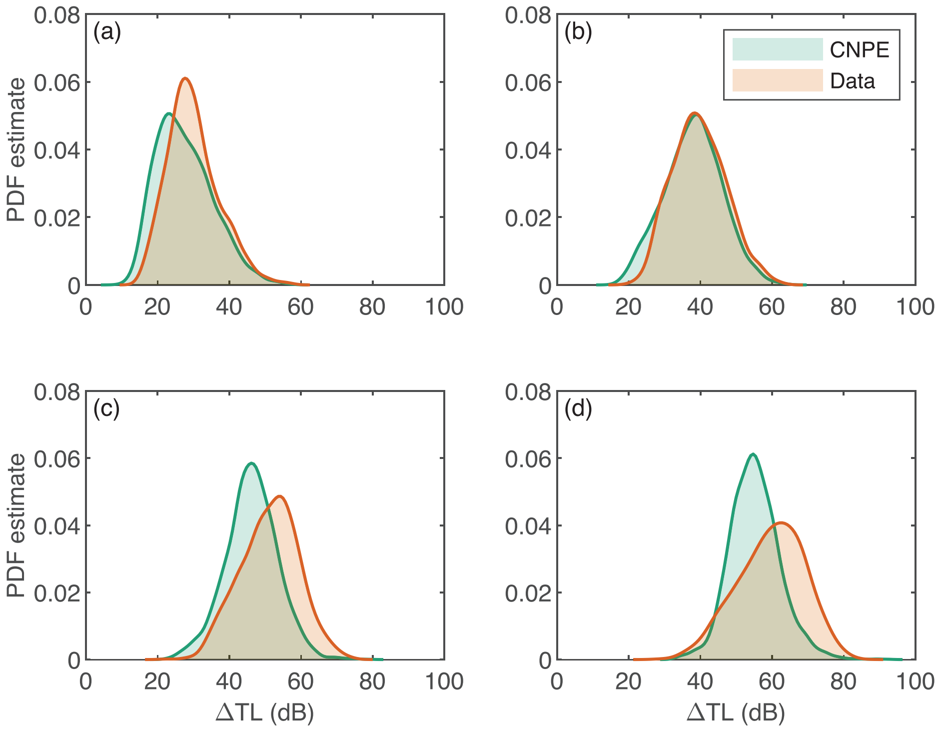

FIG. 7. (Color online) Kernel density estimates of the probability density function (PDF) for the experimental data and CNPE predictions of the TL differences (ΔTL) between the (a) 1 km, (b) 2 km, (c) 4 km, and (d) 8 km and 125 m (150 m for CNPE) ranges.

atmospheric surface layer where turning of the wind direction, nocturnal jets, and cloud layers affect sound propagation. The immediate consequence is that machine-learning models will inherit this characteristic underprediction as they are trained on the surrogate data.

Figure 8 shows the distribution of absolute errors between the machine-learning model predictions of ΔTL (Sec. III) given experimental conditions and experimental observations. The RMSEs are 9.7, 9.2, and 9.5 dB for the CW, NN, and RF models trained on the surrogate data with one realization of turbulence, respectively. The medians in error are 6.8, 6.1, and 5.5 dB for the CW, NN, and RF models (one realization of turbulence), respectively. For models trained on surrogate data with 64 realizations of turbulence, there is little difference in the median errors, although the range of outliers is greater. This is a consequence of a greater disagreement between the experimental data and simulations of propagation through 64 realizations of turbulence as opposed to propagation through a single realization of turbulence (not shown). Therefore, no substantial gains in the predictive accuracy result from increasing the number of turbulence realizations in generating the surrogate data.

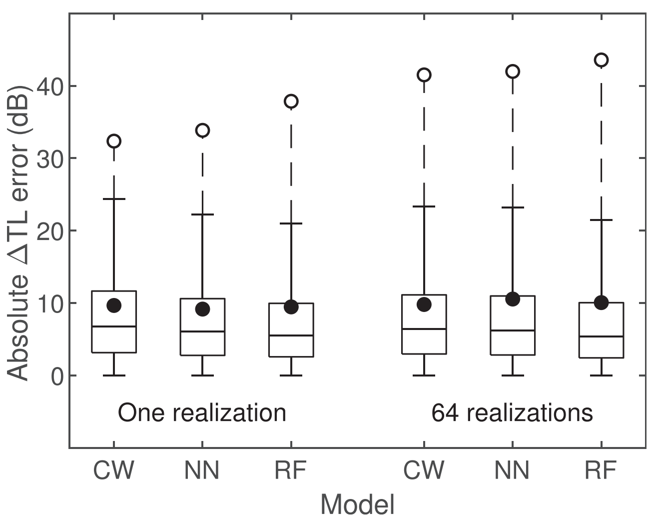

FIG. 8. The absolute error of the TL differences (ΔTL), aggregated over all cases, for the CW model, NN model, and RF model predictions versus the experimental observations. The lower, middle, and upper lines of each box are the first, second, and third quantiles, respectively. The length of the upper whisker is 1.5 times the interquartile range. The dashed lines indicate the range of outliers. The maximum outliers are indicated by open circles. The RMSE for each model in the overall grouping is shown as solid circles.

The distribution of model errors, relative to experimental observations, is more easily understood by examining the distribution of the predicted versus experimental ΔTL. Figures 9–11 show the differences among the machine-learning model predictions when trained on surrogate data with one realization of turbulence. The distribution of predictions by the CW model and NN are fairly similar with a slightly greater bias in the CW model. Although, in comparing Figs. 7 and 9, it is evident that the modes of the CW model predictions are similar to the modes of the CNPE predictions. The approximately discrete distributions at the 1 and 2 km ranges for the NN and CW models is indicative of a strongly linear relationship between the EA and range between these ranges and 125 m (not shown). The predictive distribution for the RF model most closely matches that of the surrogate data distributions in Fig. 7. The errors of the RF model will be discussed in further detail.

C. RF model errors relative to experimental observations

Figure 12 gives the RMSEs for the RF model predictions binned according to range. At a range of 1 km, the

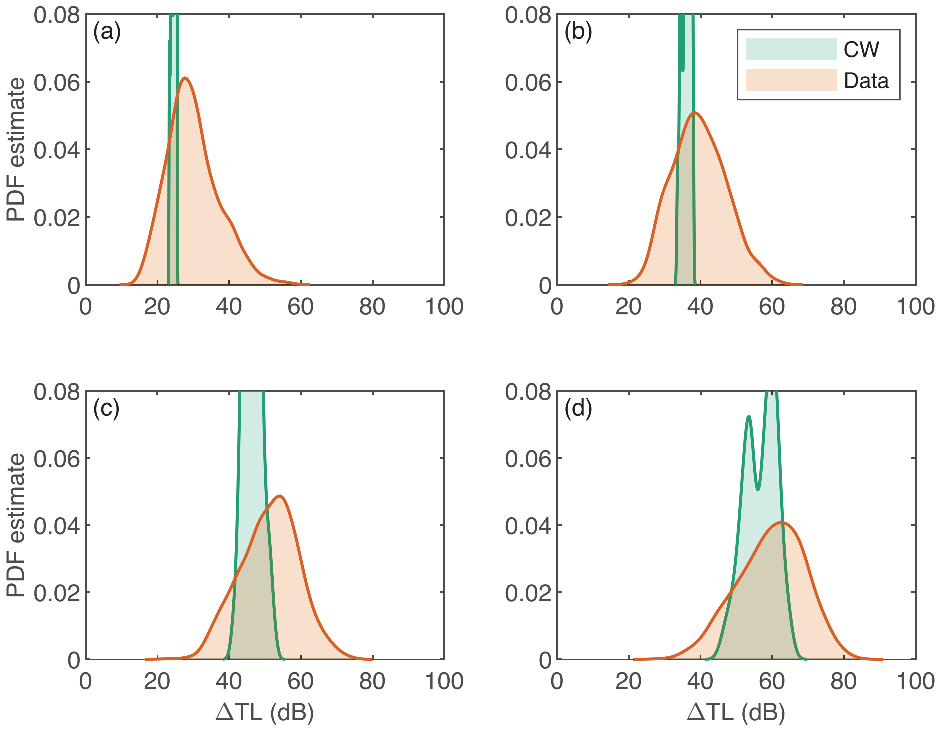

FIG. 9. (Color online) Kernel density estimates of the PDF for the experimental data and CW model predictions of the TL differences (ΔTL) between the (a) 1 km, (b) 2 km, (c) 4 km, and (d) 8 km and 125 m ranges.

RMSE is 7.2 dB and at 8 km, it is 12.6 dB. This reflects the prediction error between surrogate data and experimental observations at greater ranges, i.e., an underprediction of ΔTL by CNPE simulation as described above and shown in Fig. 7.

RMSEs binned by one-third octave band are shown in Fig. 13. No apparent trend is present in the errors. The minimum error is 7.1 dB for the 40 Hz band, and the maximum error is 12.7 dB for the 200 Hz band. Earlier work showed that typical prediction errors spanned 8–10 dB for near-ground, short duration, sound propagation due to inherent uncertainties in characterizing the environment (Wilson *et al.*, 2007). The RMSE from the RF model is consistent with the inherent random variability of the blast noise.

Errors binned by effective sound speed scale are shown in Fig. 14. The minimum error is 6.3 dB in the range of −1.0 to −0.3 m/s. The maximum error, 14.9 dB, is in the range of 0.3–1.0 m/s. By being a linear combination of the

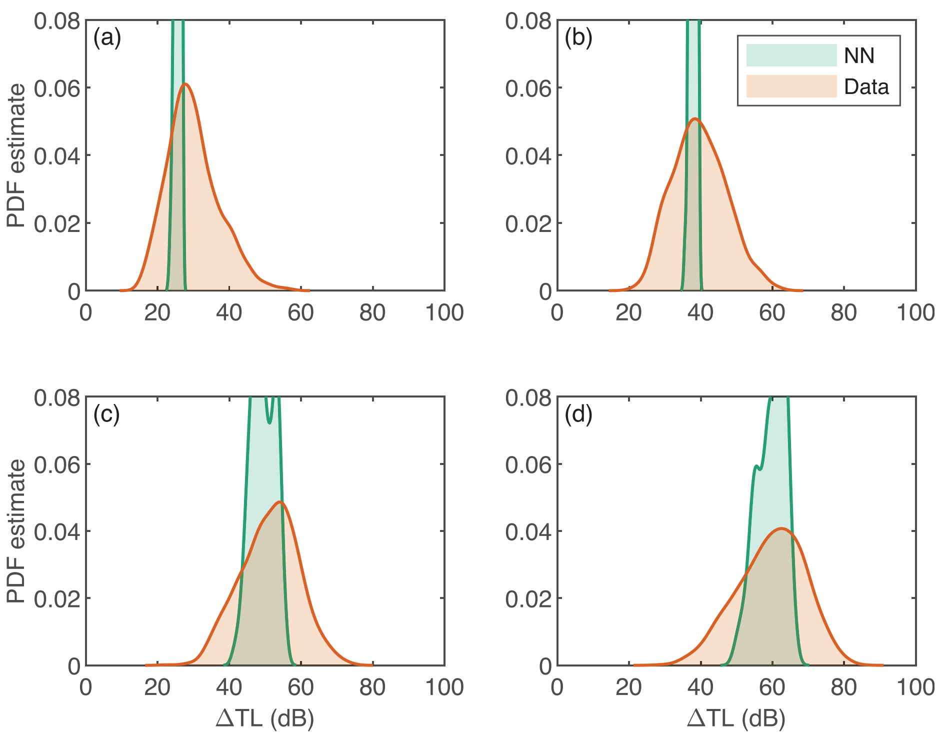

FIG. 10. (Color online) Kernel density estimates of the PDF for the experimental data and NN predictions of the TL differences (ΔTL) between the (a) 1 km, (b) 2 km, (c) 4 km, and (d) 8 km and 125 m ranges.

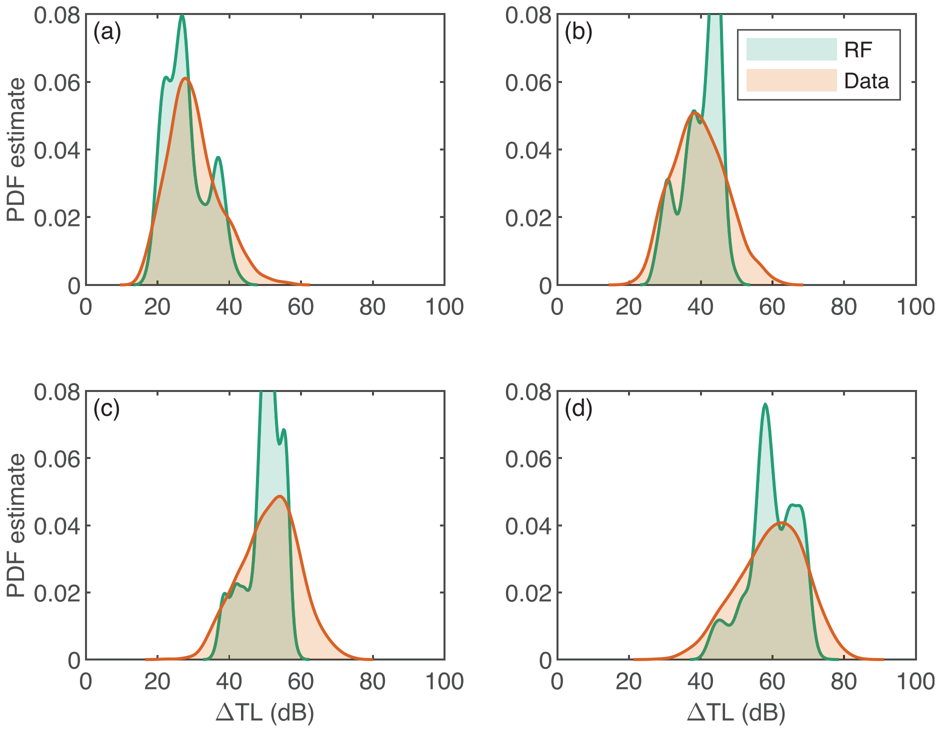

FIG. 11. (Color online) Kernel density estimates of the PDF for the experimental data and RF predictions of the TL differences (ΔTL) between the (a) 1 km, (b) 2 km, (c) 4 km, and (d) 8 km and 125 m ranges.

projected friction velocity and surface-layer temperature scale, the effective sound speed scale encapsulates the impacts of atmospheric stability as well as the directionally dependent impacts of the wind (Ostashev and Wilson, 2016, p. 95). For values below -0.3 m/s, propagation conditions can be characterized as strong to very strong upward refraction as during unstable meteorological conditions. Effective sound speed values spanning -0.3 to -0.1 m/s characterize moderate upward refraction. From -0.1 to 0.1 m/s, weak refraction prevails. Values spanning 0.1–0.3 m/s characterize moderate downward refraction. Above 0.3 m/s, propagation conditions range from strong to very strong downward refraction. Strongly downward refracting conditions tend to include those cases in which stable atmospheric stratification is present. This potentially indicates the inherent drawbacks of assuming a Monin-Obukhov profile under stable stratification in the near-ground atmosphere, which generally occurs during the nighttime. Low level jets, gravity waves, and low turbulence levels may be important environmental characteristics to capture when generating a surrogate dataset. On the other hand, unstable meteorological conditions, which typically occur during the daytime, are more accurately represented by the underlying meteorological profiles and synthetic turbulence.

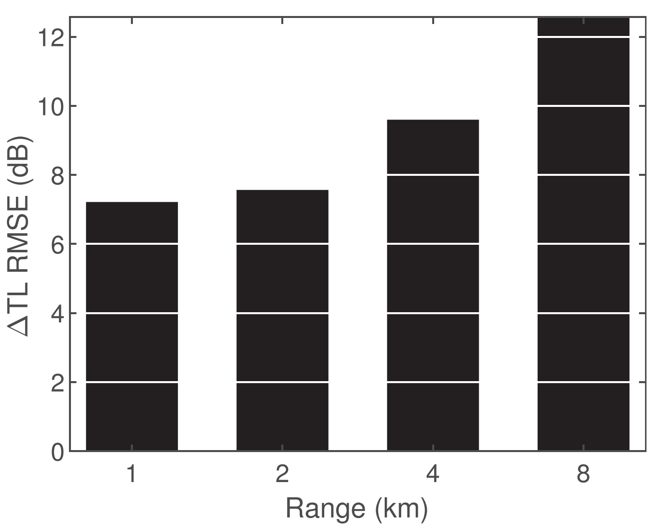

FIG. 12. The RMSE of the TL differences (ΔTL) binned by range for the RF model predictions versus experimental observations. The RF model was trained on surrogate data for a single realization of turbulence.

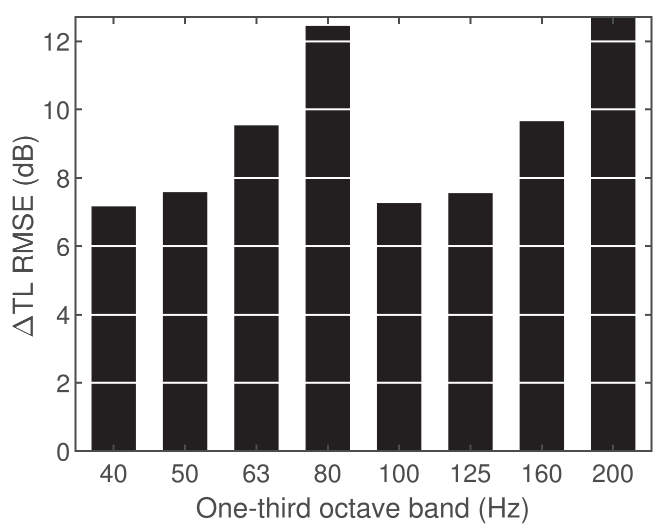

FIG. 13. The RMSE of the TL differences (ΔTL) binned by one-third octave bands for the RF model predictions versus experimental observations. The RF model was trained on surrogate data for a single realization of turbulence.

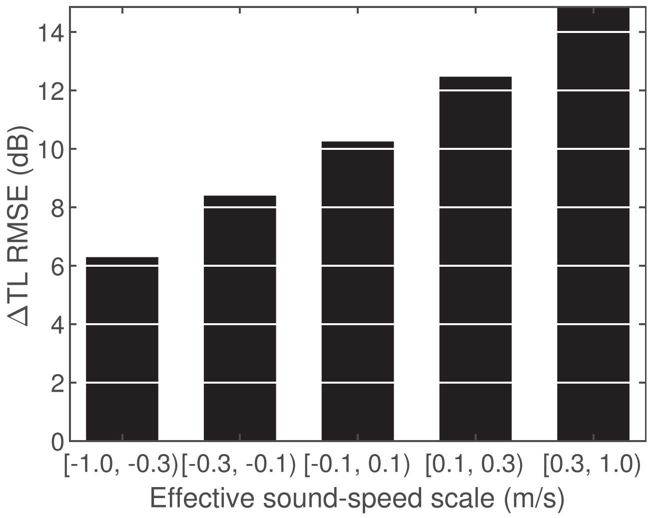

FIG. 14. The RMSE of the TL differences (ΔTL) binned by the effective sound speed scale for the RF model predictions versus experimental observations. The RF model was trained on surrogate data for a single realization of turbulence.

V. CONCLUSION

A total of 5000 different sound propagation scenarios were simulated with a high-fidelity sound propagation model over a domain of 10 km in range. Of the 1×10^6 data points collected from these simulations, approximately 70% were used to train and test machine-learning models for long-range sound propagation. Furthermore, two strategies were employed to generate the surrogate data: simulating propagation through a single realization of turbulence and simulatinnng ensemble averaged propagation through 64 realizations of turbulence.

Examination of the prediction errors and experimental errors aggregated over all of the cases and propagation conditions showed, indirectly, a greater disagreement between the experimental observations and ensemble averaged propagation simulations. Therefore, it can be concluded that it is sufficient to generate surrogate data with a single realization of turbulence. Furthermore, the quality of surrogate data is critical to generating reliably realistic machine-learning models. Underlying assumptions regarding meteorological profiles and simulated turbulence characteristics are crucial to capturing the large variance of SPLs, which is a ubiquitous feature of long-range sound propagation.

It would, of course, be preferable to train the machine-learning algorithms with experimental data if sufficiently large datasets were available. A potentially promising approach lies in physics-informed NNs, which use physics-based constraints to alleviate the need for large training datasets. Our initial efforts to employ physics-informed NNs have been moderately successful at the TL spatial features while they are less successful for the spatial details of the complex pressure field (Pettit and Wilson, 2021), apparently due to the spatial complexity of the sound field and weak dependency on the imposed physics-based loss function for the ground boundary condition.

In this study, RF models capture the variation in the surrogate data to a greater degree than CW models or NN models. A characteristic of RF models is prediction of hyper-surfaces that are not smooth. This suggests that reducing or eliminating smoothness constraints may lead to model improvements.

ACKNOWLEDGMENTS

This work was supported by the U.S. Army Engineer Research and Development Center (ERDC), Geospatial Research Engineering basic research program. We extend much appreciation to the ERDC team responsible for the measurements used in this paper. In particular, the authors thank Michael J. White (ERDC-CERL) for code that computed peak pressure and positive phase duration of C4 detonations. Any opinions expressed in this paper are those of the authors and are not to be construed as official positions of the funding agency or the Department of the Army unless so designated by other authorized documents.

Attenborough, K., Bashir, I., and Taherzadeh, S. (**2011**). "Outdoor ground impedance models," J. Acoust. Soc. Am. **129**(5), 2806–2819.
Bass, H. E. (**2003**). "Atmospheric acoustics," in *digital Encyclopedia of Applied Physics* (Wiley-VCH and Co. KGaA), pp. 145–179.
Bass, H. E., Bolen, L. N., Raspet, R., McBride, W., and Noble, J. (**1991**). "Acoustic propagation through a turbulent atmosphere: Experimental characterization," J. Acoust. Soc. Am. **90**(6), 3307–3313.
Baume, O., Gauvreau, B., Bérengier, M., Junker, F., Wackernagel, H., and Chilès, J.-P. (**2009**). "Geostatistical modeling of sound propagation: Principles and a field application experiment," J. Acoust. Soc. Am. **126**(6), 2894–2904.
Bianco, M. J., Gerstoft, P., Traer, J., Ozanich, E., Roch, M. A., Gannot, S., and Deledalle, C.-A. (**2019**). "Machine learning in acoustics: Theory and applications," J. Acoust. Soc. Am. **146**(5), 3590–3628.
Bishop, C. M. (**2006**). *Pattern Recognition and Machine Learning* (Springer, New York).
Bowman, A. W., and Azzalini, A. (**1997**). *Applied Smoothing Techniques for Data Analysis* (Oxford University Press, New York).
Breiman, L. (**2001**). "Random forests," Mach. Learn. **45**, 5–32.
Dyer, I. (**1970**). "Statistics of sound propagation in the ocean," J. Acoust. Soc. Am. **48**(1B), 337–345.
Embleton, T. F. W. (**1996**). "Tutorial on sound propagation outdoors," J. Acoust. Soc. Am. **100**(1), 31–48.
Ford, R. D., Saunders, D. J., and Kerry, G. (**1993**). "The acoustic pressure waveform from small unconfined charges of plastic explosive," J. Acoust. Soc. Am. **94**(1), 408–417.
Gershenfeld, N. (**1999**). *The Nature of Mathematical Modeling* (Cambridge University Press, Cambridge, UK), pp. 178–185.
Hart, C. R., Nykaza, E. T., and White, M. J. (**2018**). "Acoustic inversion for Monin-Obukhov similarity parameters from wind noise in a convective boundary layer," J. Acoust. Soc. Am. **144**(3), 1258–1268.
Hart, C. R., Reznicek, N. J., Wilson, D. K., Pettit, C. L., and Nykaza, E. T. (**2016**). "Comparisons between physics-based, engineering, and statistical learning models for outdoor sound propagation," J. Acoust. Soc. Am. **139**(5), 2640–2655.
Hornik, K., Stinchcombe, M., and Halbert, W. (**1989**). "Multilayer feedforward networks are universal approximators," Neural Netw. **2**(5), 359–366.
James, G., Witten, D., Hastie, T., and Tibshirani, R. (**2013**). *An Introduction to Statistical Learning: With Applications in R* (Springer, New York), pp. 176–178, 316–324.
McKay, M. D., Beckman, R. J., and Conover, W. J. (**1979**). "A comparison of three methods for selecting values of input variables in the analysis of output from a computer code," Technometrics **21**(2), 239–245.
Mungiole, M., and Wilson, D. K. (**2006**). "Prediction of outdoor sound transmission loss with an artificial neural network," Appl. Acoust. **67**(4), 324–345.

Ostashev, V. E., and Wilson, D. K. (**2016**). *Acoustics in Moving Inhomogeneous Media*, 2nd ed. (CRC Press, Boca Raton, FL), pp. 90, 95, 370–372.

Ostashev, V. E., Wilson, D. K., and Muhlestein, M. B. (**2020**). "Wave and extra-wide-angle parabolic equations for sound propagation in a moving atmosphere," J. Acoust. Soc. Am. **147**(6), 3969–3984.

Pettit, C. L., and Wilson, D. K. (**2007**). "Proper orthogonal decomposition and cluster weighted modeling for sensitivity analysis of sound propagation in the atmospheric surface layer," J. Acoust. Soc. Am. **122**(3), 1374–1390.

Pettit, C. L., and Wilson, D. K. (**2020**). "A physics-informed neural network for sound propagation in the atmospheric boundary layer," Proc. Mtgs. Acoust. **42**(1), 022002.

Salomons, E. M. (**2001**). *Computational Atmospheric Acoustics* (Kluwer Academic, Dordrecht, The Netherlands).

Valente, D., Ronsse, L. M., Pater, L., White, M. J., Serwy, R., Nykaza, E. T., Swearingen, M. E., and Albert, D. G. (**2012**). "Blast noise characteristics as a function of distance for temperate and desert climates," J. Acoust. Soc. Am. **132**(1), 216–227.

West, M., Gilbert, K., and Sack, R. A. (**1992**). "A tutorial on the parabolic equation (PE) model used for long range sound propagation in the atmosphere," Appl. Acoust. **37**(1), 31–49.

Wilson, D. K. (**1993**). "Relaxation-matched modeling of propagation through porous media, including fractal pore structure," J. Acoust. Soc. Am. **94**(2), 1136–1145.

Wilson, D. K. (**2000**). "A turbulence spectral model for sound propagation in the atmosphere that incorporates shear and buoyancy forcings," J. Acoust. Soc. Am. **108**(5), 2021–2038.

Wilson, D. K., Andreas, E. L., Weatherly, J. W., Patton, E. G., and Sullivan, P. P. (**2007**). "Characterization of uncertainty in outdoor sound propagation predictions," J. Acoust. Soc. Am. **121**(5), EL177–EL183.

Wilson, D. K., Brasseur, J. G., and Gilbert, K. E. (**1999**). "Acoustic scattering and the spectrum of atmospheric turbulence," J. Acoust. Soc. Am. **105**(1), 30–34.

Wilson, D. K., Ostashev, V. E., and Lewis, M. S. (**2009**). "Moment-screen method for wave propagation in a refractive medium with random scattering," Wave Random Complex **19**(3), 369–391.

Wilson, D. K., Pettit, C. L., and Ostashev, V. E. (**2015**). "Sound propagation in the atmospheric boundary layer," Acoust. Today **11**(2), 44–53.

Wyngaard, J. C. (**2010**). *Turbulence in the Atmosphere* (Cambridge University Press, Cambridge, UK).

REPORT DOCUMENTATION PAGE

Form Approved OMB No. 0704-0188

1. REPORT DATE *(DD-MM-YYYY)*
July 2021

2. REPORT TYPE
Final

3. DATES COVERED *(From - To)*

4. TITLE AND SUBTITLE
Machine-learning of long-range sound propagation through simulated atmospheric turbulence

5a. CONTRACT NUMBER

5b. GRANT NUMBER

5c. PROGRAM ELEMENT NUMBER
611102

6. AUTHOR(S)
Carl R. Hart, D. Keith Wilson, Chris L. Pettit, and Edward T. Nykaza

5d. PROJECT NUMBER
AB2

5e. TASK NUMBER
01

5f. WORK UNIT NUMBER

7. PERFORMING ORGANIZATION NAME(S) AND ADDRESS(ES)
See next page.

8. PERFORMING ORGANIZATION REPORT NUMBER
ERDC MP-21-7

9. SPONSORING / MONITORING AGENCY NAME(S) AND ADDRESS(ES)
U.S. Army Corps of Engineers
441 G Street NW
Washington, DC 20314

10. SPONSOR/MONITOR'S ACRONYM(S)
USACE

11. SPONSOR/MONITOR'S REPORT NUMBER(S)

12. DISTRIBUTION / AVAILABILITY STATEMENT
Approved for public release; distribution is unlimited.

13. SUPPLEMENTARY NOTES
This article was originally published online in the *Journal of the Acoustical Society of America* on 21 June 2021. This paper is part of a special issue on Machine Learning in Acoustics.

14. ABSTRACT

Conventional numerical methods can capture the inherent variability of long-range outdoor sound propagation. However, computational memory and time requirements are high. In contrast, machine-learning models provide very fast predictions. This comes by learning from experimental observations or surrogate data. Yet, it is unknown what type of surrogate data is most suitable for machine-learning. This study used a Crank-Nicholson parabolic equation (CNPE) for generating the surrogate data. The CNPE input data were sampled by the Latin hypercube technique. Two separate datasets comprised 5000 samples of model input. The first dataset consisted of transmission loss (TL) fields for single realizations of turbulence. The second dataset consisted of average TL fields for 64 realizations of turbulence. Three machine-learning algorithms were applied to each dataset, namely, ensemble decision trees, neural networks, and cluster-weighted models. Observational data come from a long-range (out to 8 km) sound propagation experiment. In comparison to the experimental observations, regression predictions have 5–7 dB in median absolute error. Surrogate data quality depends on an accurate characterization of refractive and scattering conditions. Predictions obtained through a single realization of turbulence agree better with the experimental observations.

15. SUBJECT TERMS
Machine learning; Sound – Propagation; Sound -- Transmission – Measurement; Noise –Measurement; Acousitcal eningeering – Analysis; Differential equations, Partial

16. SECURITY CLASSIFICATION OF: a. REPORT	b. ABSTRACT	c. THIS PAGE	17. LIMITATION OF ABSTRACT	18. NUMBER OF PAGES	19a. NAME OF RESPONSIBLE PERSON / 19b. TELEPHONE NUMBER *(include area code)*
Unclassified	Unclassified	Unclassified	UU	18	

7. PERFORMING ORGANIZATION NAME(S) AND ADDRESS(ES)

Cold Regions Research and Engineering
U.S. Army Engineer Research and Development Center
72 Lyme Road
Hanover, NH 07355

Aerospace Engineering Department
U.S. Naval Academy
Annapolis, MD 21402

Construction Engineering Research Laboratory
U.S. Army Engineer Research and Development Center
2902 Newmark Drive
Champaign, IL 61822